Reports

Evidence for Sediment Eruption on Deep Sea Floor, Gulf of Mexico

DAVID B. PRIOR, EARL H. DOYLE, MICHAEL J. KALUZA

A large crater has been discovered on the sea floor, Gulf of Mexico, in a water depth of 2176 meters. Deep-tow high-resolution imagery shows that the crater is cut into a low hill surrounded by near-surface concentric faults. Approximately 2 million cubic meters of ejected sediment forms a peripheral debris field. The low hill and faults may be related to mud diapirism or intrusion of gas hydrates into near-surface sediments. A recent eruption evacuated sediments from the crater, apparently because of release of overpressured petrogenic gas.

THE WORLD'S OCEAN FLOORS ARE affected by various high-energy sediment transport processes, such as turbidity currents, debris flows, slides, and benthic storms [for example (*1–4*)]. These processes affect sedimentation patterns and can be hazardous to sea-floor engineering. During recent high-resolution geophysical surveying in the Gulf of Mexico, we discovered a large crater and neighboring debris field. The bottom features indicate that local sediment eruptions may also be significant, natural, high-energy phenomena.

Deep-tow acoustic imagery revealed a large, fresh, elliptical crater (58 m deep, 280 m across, and 400 m long) in a water depth of 2176 m (Fig. 1). Approximately 2×10^6 m^3 of sediment has been evacuated. A surrounding debris field extends up to 430 m from the crater and is composed of blocky fragments of sediment. The crater is located 115 km southeast of the Mississippi River delta on the lower continental slope (28°16'46"N, 88°8'5"W).

The regional sea-floor topography has a maximum relief of about 200 m. Shale and salt diapirs buried under more than 900 m of Pleistocene and Holocene sediments (*5*) have formed broad domes and basins (5 to 7 km across) on the sea floor. The top of the sediment sequence consists of 50 to 100 m of upper Pleistocene parallel-bedded deposits. Dating of cores from a similar setting 35 km to the northwest indicates that the Holocene deposition rate was 2 to 3 m per 10,000 years.

Deeply towed 100-kHz side-scan sonar (200-m range) and 3.5-kHz subbottom profiler sensors are routinely used to survey bottom morphology and geologic structures (*6*). The crater could not be seen with surface-deployed geophysical equipment because of beam spreading and signal attenuation effects. The deep-tow side-scan sonar mosaic (Figs. 1 and 2) and subbottom profiles (Fig. 3, A and B) allowed construction of a three-dimensional interpretation of the crater and related geologic features (Fig. 4).

The crater is located on the west side of a low hill, much of which was destroyed during sediment evacuation. The near-surface parallel-bedded sediments forming the hill are domed upward and truncated by the crater walls (Fig. 3A). The crater floor lies about 65 to 70 m below the original hilltop and ~40 m below the surrounding sea floor. The sidewalls of the crater are steep (23°) and have sharp, slightly irregular crests. Several small gullies separated by ridges lead upward toward the west, where the crater lip is lowest. Subtle sediment splays radiate away from the ends of the gullies on the crater rim. Debris ejected from the crater forms a lobate apron over the lower western slopes of the hill (Figs. 2, 3B, and 4). The ejecta field extends 430 m south and west of the crater and has several different components. Distally, the debris forms thinning

D. B. Prior, Coastal Studies Institute and Department of Geology and Geophysics, Louisiana State University, Baton Rouge, LA 70803.
E. H. Doyle, Shell Oil Company, Post Office Box 2099, Houston, TX 77001.
M. J. Kaluza, Fugro-McClelland, Inc., Post Office Box 740010, Houston, TX 77274.

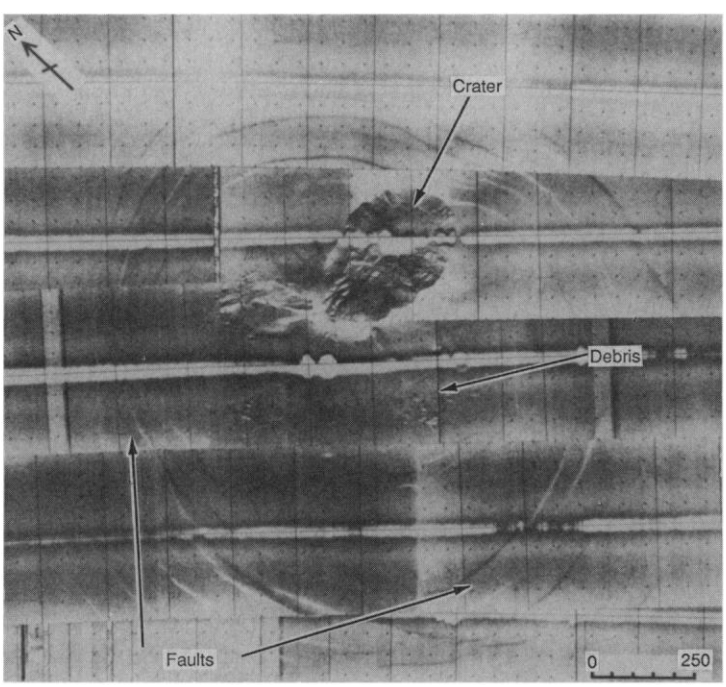

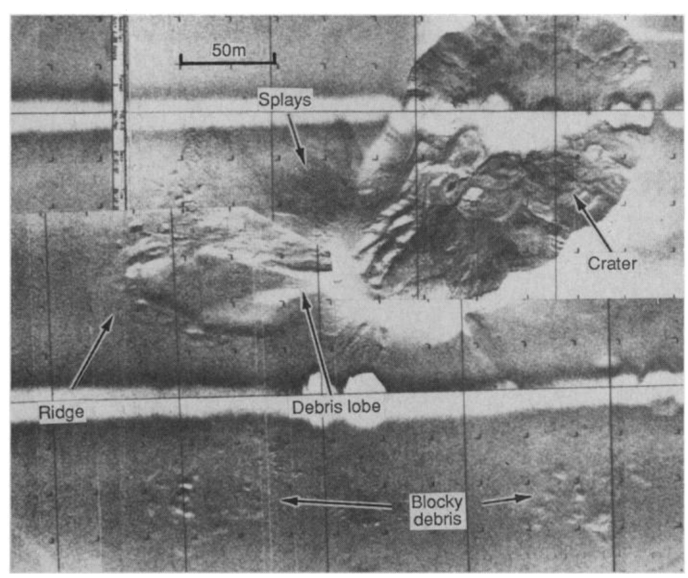

Fig. 1. (Left) Composite side-scan sonar mosaic of sea-floor crater, debris field, and concentric faults. Scale in meters. **Fig. 2.** (Right) Close-up side-scan sonar image of crater and debris field.

wedges of acoustically opaque material that onlap the bedded sediments (Fig. 3B). Large pieces of sediment evacuated from the crater are scattered throughout the depositional area. Individual blocks are up to 35 m across. Close to the western lip, a debris lobe emanates from the lowest part of the crater rim, near the foot of the hill slope, and extends 200 to 250 m to the northwest (Figs. 2 and 4). A low, rounded pressure ridge surrounds the outer margins of the lobe, with peripheral concentrations of blocks.

Near circular, concentric patterns of sea-floor steps or low scarps with relief of 1 to 3 m surround the hill, crater, and debris field (Figs. 1 and 4). Subbottom profiles (Fig. 3, A and B) reveal that the scarps are the result of near-surface, normal faulting around the low hill. The faults, which locally form grabens, extend only to depths of 30 to 40 m and have produced maximum offsets of 3 to 4 m.

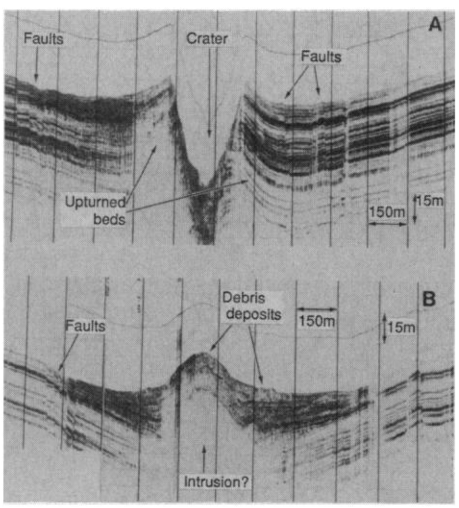

Fig. 3. (**A**) Subbottom profile (3.5 kHz) across the crater and peripheral faults (location is shown on Figs. 1 and 4). (**B**) Subbottom profile (3.5 kHz) across some of the debris flow from the crater (location is shown on Figs. 1. and 4).

The crater and associated features are located above a deep fault zone on the flank of one of the subsurface shale or salt diapirs (Fig. 5). The faults have formed a graben in the sediments below the crater but do not reach the sea floor. The subsurface faults are partly obscured by two laterally extensive zones of high-amplitude seismic reflections at depths of 75 and 250 m. The high-amplitude reflections extend over the diapir crest and are most distinctive where they intersect the subsurface faults.

The flanks of diapirs are well-known hydrocarbon traps in the Gulf of Mexico. Faulting commonly allows hydrocarbons, especially gas, to migrate upward and to permeate overlying sediments. The high-amplitude zones associated with the subsurface faults and in the sediments above the diapir may be areas that contain hydrocarbons. The low hill, crater, and surrounding faults thus apparently lie directly above a region of petrogenic gas seepage. The water depth (2176 m) where these features occur is well within the theoretical temperature and depth limits for near-surface hydrate formation [for example (*7*)]. In the Gulf of Mexico, seepage of petrogenic fluids leads to hydrates at or near the sea floor in water depths greater than 500 m. Mounds up to 40 m high with surface hydrate–sediment mixtures have been identified in cores (*8*–*10*).

The development of the hill and concentric faults involved local deformation of the near-surface sediments over an area of about 1.5×10^6 m^2. The shallow beds have been pushed upward to form the hill, an activity associated with peripheral faulting and subsidence. The deeper beds were unaffected by

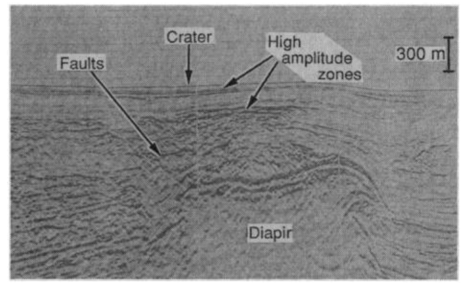

Fig. 5. Multichannel seismic profile oriented north-northwest–south-southeast approximately 1000 m east of the crater.

the uplift. The deformation geometry requires an intrusive force immediately below the hill and tensional stresses in the surrounding area. The exact mechanism of intrusion cannot be determined solely from the acoustic data but is probably related to upward seepage of hydrocarbons; areas with mounds of gas-rich mud or mud diapirs formed by flowage of sediment and gas mixtures are common sea-floor features in the Gulf of Mexico (*10*–*12*). Alternatively, the growth of gas hydrates in the near-surface sediment could have formed the hill by local expansion of sediment, water, and hydrate mixtures. An analogy is the development of some arctic ice-cored hills. Pingos commonly have comparable morphology (*13*).

Crater formation subsequently removed much of the hill. The debris lobe and pressure ridge on the west side suggest that initially sliding may have occurred on the oversteepened hillside. As the crater deepened the scattered blocks and splays were emplaced by both outward and upward sediment transport. The final depth of the crater, the size of the largest blocks, long transport distances, and upward sediment movement to the surrounding sea floor all suggest highly energetic conditions. The crater geometry and debris field are similar to features produced by violent, drilling-induced gas blowouts (*14*). The features are, however, quite different from subtle pockmarks ascribed to gradual gas venting and sediment resuspension (*15*). Thus, natural rapid release of large volumes of overpressured gas appears to be the most likely explanation for the crater and ejected debris. Catastrophic venting could have been the result of high-pressure surges from the hydrocarbon reservoir. Alternatively, development of a relatively impermeable hydrate layer in the near-surface zone, above a source of gas seepage, could have led to a local buildup of pressurized gas. Tensional rupturing of the hilltop or sliding of sediments off the slopes may have triggered release.

The precise date for crater formation is

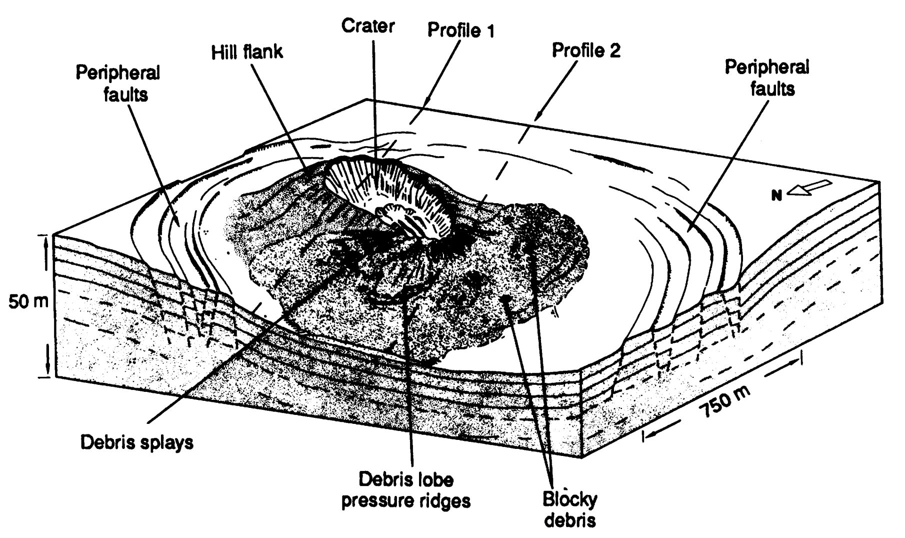

Fig. 4. Interpretive three-dimensional schematic diagram of the sea floor and near-surface features. Profile 1 is Fig. 3A and profile 2 is Fig. 3B.

not known. The subbottom profile data show that the most recently deposited Holocene sediments are truncated by the crater (Fig. 3A). There is no evidence of a recent sediment drape over the deposits (Figs. 2 and 3B). The crater rim, internal walls, and debris field appear fresh (Fig. 2). Erosion or smoothing by bottom currents is not apparent. Together, the evidence suggests that the crater formed recently, probably within a few hundred years. An unusual sea-surface disturbance (possibly gas venting) was observed in the same vicinity in September 1906, but it is not possible to link this event with formation of the crater (*16*).

Hydrocarbon seepage is a relatively common process in the Gulf of Mexico, accounting for various phenomena such as gas-rich sediments hydrates, mud diapirs, and water column anomalies (*9, 10, 17, 18*). Release is usually gradual, but may be persistent (*18*). One example of natural high-energy venting was reported in 1200-m water depth (*16*). Also, a crater (about 40 m deep, 500 m in diameter) was tentatively recognized from a single acoustic profile in a water depth of 900 m (*19*). The high-resolution, deep-tow data now indicate that blowout-type craters and ejecta fields can form naturally in deep water following intrusive deformation of the sea floor.

REFERENCES AND NOTES

1. D. Prior *et al.*, *Science* **237**, 1330 (1987).
2. D. Prior and J. Coleman, in *Marine Slides and Other Mass Movements*, S. Saxov and J. Nieuwenhuis, Eds. (Plenum, New York, 1982), pp. 21–49.
3. K. Karlsrud and L. Edgers, in *ibid.*, pp. 61–68.
4. C. Hollister and N. McCave, *Nature* **309**, 220 (1984).
5. R. Martin and A. Bouma, *Mar. Geotech.* **5**, 63 (1982).
6. D. Prior *et al.*, *Proceedings of the Twentieth Offshore Technology Conference, OTC 5758*, 2 to 5 May 1988 (OTC, Houston, TX, 1988).
7. S. Miller, in *Natural Gases in Marine Sediments*, I. Kaplan, Ed. (Plenum, New York, 1974), pp. 151–177.
8. K. Campbell, J. Hooper, D. Prior, *Proceedings of the Eighteenth Offshore Technology Conference, OTC 5105*, 5 to 8 May 1986 (OTC, Houston, TX, 1986).
9. T. W. Neurater, thesis, Texas A&M University, 1988.
10. J. W. Brooks and W. Bryant, *Geological and Geochemical Implications of Gas Hydrates in the Gulf of Mexico* (Department of Energy, Morgantown, PA, 1985).
11. L. Roemer and W. Bryant, *Texas A&M Tech. Rep. 77-4-T* (1977).
12. T. Ferebee and W. Bryant, *ibid. 79-4-T* (1979).
13. J. Mackay, *Can. J. Earth Sci.* **24**, 1108 (1987).
14. W. Bryant and L. Roemer, in *Handbook of Geophysical Exploration at Sea*, R. Geyer, Ed. (CRC Press, Boca Raton, FL, 1983), pp. 123–186.
15. R. McQuillin *et al.*, *Inst. Geol. Sci. Rep. 90* (1979).
16. J. Soley, *Sci. Am. Suppl.* **1788**, 229 (1910).
17. B. Bernard *et al.*, *Earth Planet. Sci. Lett.* **31**, 48 (1976).
18. W. Sweet, *Am. Assoc. Petrol. Geol. Bull.* **58**, 1133 (1974).
19. T. Ferebee, Jr., thesis, Texas A&M University (1978).
20. We thank Shell Offshore Inc. for permission to use recently acquired data.

2 September 1988; accepted 28 November 1988

Rhenium-Osmium Isotope Systematics of Carbonaceous Chondrites

R. J. Walker and J. W. Morgan

Rhenium and osmium concentrations and Os isotopic compositions of eight carbonaceous chondrites, one LL3 ordinary chondrite, and two iron meteorites were determined by resonance ionization mass spectrometry. Iron meteorite ^{187}Re/^{186}Os and ^{187}Os/^{186}Os ratios plot on the previously determined iron meteorite isochron, but most chondrite data plot 1 to 2 percent above this meteorite isochron. This suggests either that irons have significantly younger Re-Os closure ages than chondrites or that chondrites were formed from precursor materials with different chemical histories from the precursors of irons. Some samples of Semarkona (LL3) and Murray (C2M) meteorites plot 4 to 6 percent above the iron meteorite isochron, well above the field delineated by other chondrites. Murray may have lost Re by aqueous leaching during its preterrestrial history. Semarkona could have experienced a similar loss of Re, but only slight aqueous alteration is evident in the meteorite. Therefore, the isotopic composition of Semarkona could reflect assembly of isotopically heterogeneous components subsequent to 4.55 billion years ago or Os isotopic heterogeneities in the primordial solar nebula.

Because Re and Os are highly refractory and siderophile elements, the Re-Os isotope system is particularly important in studies concerned with metal phases and high-temperature inclusions of meteorites. Potential applications of the system include dating meteorites, especially with respect to the chronology of the assembly and subsequent metamorphism of genetically disparate components, and providing estimates of the initial Os isotopic composition and Re/Os ratio of the early earth. This ratio is an important chemical tracer for understanding the formation of the earth's core and the chemical evolution of the mantle and crust. Because of analytical limitations, most Re-Os isotopic analyses of meteorites have been obtained from those metal phases that concentrated Re and Os (*1–3*). Data for IA, IIA, IIIA, and IVB iron meteorites define a line on a ^{187}Re/^{186}Os versus ^{187}Os/^{186}Os plot. Geochronologic applications, however, have been hindered by the lack of an accurate determination of the ^{187}Re half-life. Herr and co-workers (*3*) concluded that iron meteorites crystallized between 4 and 5 billion years ago (Ga) using a ^{187}Re half-life of $(4.3 \pm 0.5) \times 10^{10}$ years that was based on terrestrial molybdenite data (*4*). More recently, iron meteorites and metal separates from ordinary chondrites have been examined with secondary ion mass spectrometry (*1, 2*). A ^{187}Re half-life of $(4.56 \pm 0.12) \times 10^{10}$ years was derived with the assumption that chondrites and irons have a common age of 4.55 Ga. This result is within uncertainty of the half-life estimated from molybdenites and also of a value of $(4.36 \pm 0.13) \times 10^{10}$ years based on the laboratory determination of the growth of ^{187}Os in highly purified $HReO_4$ (*5*). Recent refinements of the laboratory determination, however, have yielded a half-life of $(4.23 \pm 0.13) \times 10^{10}$ years (*6*), which is significantly less than the meteorite-derived half-life.

We have measured the Re and Os concentration and Os isotopic composition for whole rock samples of eight carbonaceous chondrites and the unequilibrated LL3 ordinary chondrite Semarkona, as well as two iron meteorites. Chondrites represent one of the least distorted samples of the compositional and isotopic characteristics of the primordial solar nebula and thus provide information regarding the initial isotopic composition of Os in the early solar system.

We dissolved and equilibrated the samples (*7–9*) with enriched ^{190}Os and ^{185}Re spikes by alkaline fusion. Osmium was distilled twice as OsO_4 from H_2SO_4-H_2O_2 solution; Re was recovered from the residual solution by anion exchange. Both Re and Os were further purified by adsorption onto anion exchange beads and loaded onto a Ta filament. Total analytical blanks were <70 pg for Re and <20 pg for Os. Four Os isotopic ratios were measured with a resonance ionization mass spectrometer (*10*): ^{190}Os to ^{192}Os for determination of Os concentration by isotope dilution (ID); ^{192}Os to ^{188}Os for correction for mass fractionation, typically <1% per mass; and ^{192}Os to ^{187}Os and ^{188}Os to ^{187}Os for measurement of the relative abundance of ^{187}Os. These ratios were converted to ^{187}Os/^{186}Os, the most commonly reported ratio, with ^{192}Os/^{186}Os and ^{188}Os/^{186}Os values of 25.59 and 8.302, re-

R. J. Walker, Department of Terrestrial Magnetism, Carnegie Institution of Washington, 5241 Broad Branch Road, NW, Washington, DC 20015.
J. W. Morgan, U.S. Geological Survey, Mail Stop 981, Reston, VA 22092.